Advices derived from troubleshooting a sensor-based adaptive optics direct stochastic optical reconstruction microscope

Final report for the module
Advanced Lab Rotation II

Written by: Lennart Groß

Date: 19/04/2022
Module duration: 01/03/2021 – 20/06/2021
Program: MSc Translational Neuroscience

UK
Supervisors: Prof Martin Booth
Dr Jingyu Wang
Laboratory: Dynamic Optics and Photonics Group
Department of Engineering Science
University of Oxford

DE
Supervisors: Prof Markus Sauer
Dr Gerti Beliu
Laboratory: Biotechnology and Biophysics
Biocenter
University of Würzburg

Layout and language edited on 30/10/2022.

Abstract

One rarely finds practical guidelines for the implementation of complex optical setups. Here, we aim to provide technical details on the decision making of building and revising a custom sensor-based adaptive optics (AO) direct stochastic optical reconstruction microscope (*d*STORM) to provide practical assistance in setting up or troubleshooting similar devices.
The foundation of this report is an instrument constructed as part of a master's thesis in 2021, which was built for deep tissue imaging [1]. The setup is presented in the following way: (1) An optical and mechanical overview of the system at the beginning of this internship is given. (2) The optical components are described in detail in the order at which the light passes through, highlighting their working principle and implementation in the system. The optical component include (2A) a focus on even sample illumination, (2B) restoring telecentricity when working with commercial microscope bodies, (2C) the AO elements, namely the deformable mirror (DM) and the wavefront sensor, and their integration, and (2D) the separation of wavefront and image capture using fluorescent beads and a dichroic mirror. After addressing the limitations of the existing setup, modification options are derived. The modifications include the implementation of adjustment only light paths to improve system stability and revise the degrees of freedom of the components and changes in lens choices to meet the specifications of the AO components. Last, the capabilities of the modified setup are presented and discussed: (1) First, we enable epifluorescence imaging of bead samples through 180 µm unstained murine hippocampal tissue with wavefront error correction of $\approx 90\,\%$. Point spread function, wavefront shape and Zernike decomposition of bead samples are presented. (2) Second, we move from epifluorescent to *d*STORM imaging of tubulin stained primary mouse hippocampal cells, which are imaged through up to 180 µm of unstained murine hippocampal tissue. We show that full width at half maximum (FWHM) of prominent features can be reduced in size by nearly a magnitude from uncorrected epiflourescence images to *d*STORM images corrected by the adaptive optics. We present *d*STORM localization count and FWHM of prominent features as as a function of imaging depth.

Introduction

In adaptive optics (AO) direct stochastic optical reconstruction microscopy (*d*STORM), two techniques are combined to reach super-resolution imaging in non-superficial planes of samples having a non-homogenous distribution of refractive indices. (1) In *d*STORM, fluorophores on the sample are turned into a non-emissive dark state by exposure to high laser power density. Randomly, fluorophores can spontaneously recover and emit light for a short amount of time before going back into the dark state, creating a blinking of the sample. By recording a time lapse, the few and spread out fluorophores in each frame can be fitted with a Gaussian to reconstruct their position with sub-diffraction resolution. [2, 3, 4] (2) AO is a technique of shaping the wavefront of the emission light to recover from optical aberrations induced by the sample. [5, 6, 7]

Optical layout overview The system utilizes a Nikon Ti-Eclipse (Ti-E), a commercially available infinity-corrected inverted research microscope body. [8] Using a commercial microscope body arose from the following considerations: (1) A stable, motorized stage and objective lens mount as well as a perfect focus system (PFS) are guaranteed. The PFS corrects drifting motions to keep the focal plane in the sample steady. (3) Nikon ships an extended imaging software (NIS Elements [9]) with its microscopes, enabling automation of complex imaging procedures.
The optical paths are designed for an infinity-corrected apochromatic objective lens (Nikon SR HP Plan Apo 100X/1.35 Sil λS, L_{obj}). [10] The objective lens has a magnification of $100\times$, a numerical aperture (NA) of 1.35 and uses silicone oil as the immersion medium.

The system was set up on an optical table and an overview is given in Figure 1. Two excitation lasers are used (488 nm, 640 nm). The excitation beams are combined using a dichroic filter DC_2 and aligned to the optical axis of the HILO/TIRF rail. HILO and TIRF and the use of the HILO/TIRF rail are explained in the following paragraph. On the HILO/TIRF rail, two lenses are mounted, followed by a right-angle mirror, to direct the laser beam into the microscope body and focus it onto the back focal plane of the objective lens.
Fluorescence from the sample is collected and collimated by the objective lens L_{obj}. The tube lens L_{tube} focuses the light to the first image plane, which is formed right outside the microscope body. In the image plane, a field lens L_{field} is placed to correct the missing image-side telecentricity of the Nikon Ti-E. Lens L_1 collimates the light again and forms the second Fourier plane, where a Thorlabs DMP-40 piezoelectric deformable mirror (DM) is placed. The light from the DM is split by the dichroic filter at 647 nm. The red side of the spectrum is focused onto the Andor Sona B4.2 camera, while the blue part is expanded by the lenses L_{S1} and L_{S2} to create another Fourier plane for the Thorlabs WFS-30 Shack-Hartman Wavefront Sensor (SH). Specifications for the components can be found in the supplementary material.

Using HILO illumination to reach a high light density deep inside the sample To archive a widefield illumination, the excitation beam is focused onto the back focal plane of the objective. Thereby, the excitation light exits the objective lens as a straight, collimated beam. When sliding the HILO/TIRF rail along its optical axis, the focus spot shifts from the center of the objective's back focal plan to its periphery. This inclines the collimated

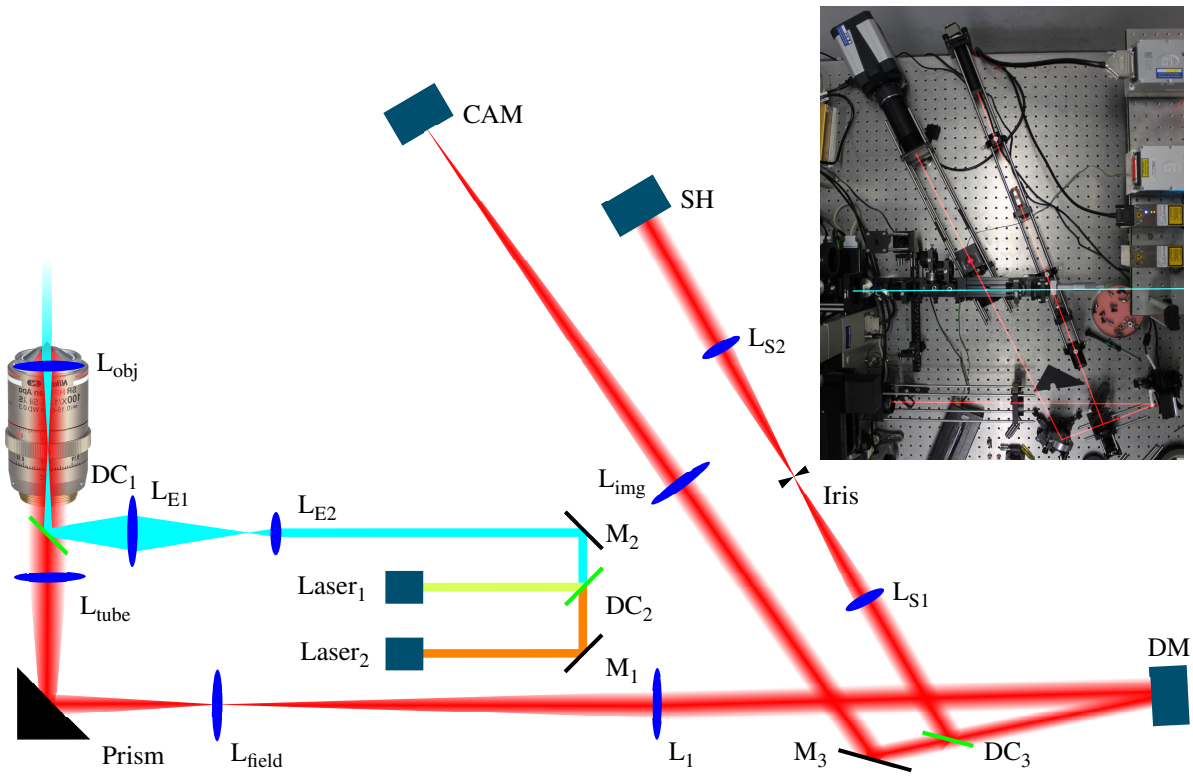

Figure 1: Schematic of the light paths of the initial adaptive optics microscope setup with DM and SH as the starting point for the internship. The excitation path from the laser to the specimen is shown in light blue. The emission path from the specimen to the camera (CAM) and to the Shack-Hartmann wavefront sensor (SH) is shown in red. Lenses are marked in dark blue, mirrors and reflective prisms are shown in black. Dichroic filters (DF) are marked in green. The objective and the magnification of the lenses is not to scale.
Insert: Photograph of the setup. Taken from Groß [1]

excitation beam, making it thinner and thereby increasing light density. As only a (inclined) sheet of the sample is illuminated, this strongly reduces background. This technique is called Highly Inclined and Laminated Optical sheet (HILO) illumination. [11] When increasing the inclination angle, light will eventually undergo total internal reflection at the interface between the cover glass and the sample, and the evanescent wave emerging into the sample can be used as excitation light instead. This technique is called Total Internal Reflection Fluorescence (TIRF). [12] While TIRF provides a higher signal to noise (SN) ratio compared to HILO due to the short penetration depth of the evanescent wave ($\approx$ 100 nm), this also limits its application to superficial planes. Therefore, the illumination was provided in the HILO regime with varying inclinations depending on the depth of the image plane below the sample surface.

Restoring image-side telecentricity using a field lens
By combining two lenses, a point-like object located in the focal spot of the first lens ("objective lens") will be imaged into the focal spot of the second lens "tube lens", regardless of the distance between the two lenses. This is true as long as the object is placed in the focus spot on the optical axis, as all rays between the lenses then become parallel (Figure 2A, in blue).
However, the matter changes when a second point source is introduced, which is not located on the optical axis of the system. This is the common case when resolving finitely extended samples (Figure 2A, in red) Three cases can be distinguished:
(1) (full) telecentricity: The lenses only relay both points back to its original relative position, if the two lenses are separated by the sum of their focal lengths (Figure 2A). In microscopes, this space between the lenses is often called tube length or infinity space. If the tube length equals the sum of the focal lengths, the system is called telecentric. If you change the focus of such system, the magnification will not change, because the light cones, defined by the converging light that belongs to one point emitter in the sample, coming from the tube lens and forming the image are parallel.
(2) object-side telecentricity: If the stop position stays f_{obj} away from the objective lens, and the tube lens is moved closed to the objective lens, the cone of light coming from the tube lens to form the off-centered image point will bend outwards (Figure 2B). If the tube lens is moved further apart from the objective lens, the light cones will bend inwards (Figure 2C). As a result, the two points are imaged further apart or closer together, resulting in the image being magnified or demagnified. In such setups, which are called object-side telecentric, a change in focus on the object side always results in a change in magnification of the image. As camera positions are usually fixed, this can be used in imaging applications.
(3) image-side telecentricity: If the lenses stay the same

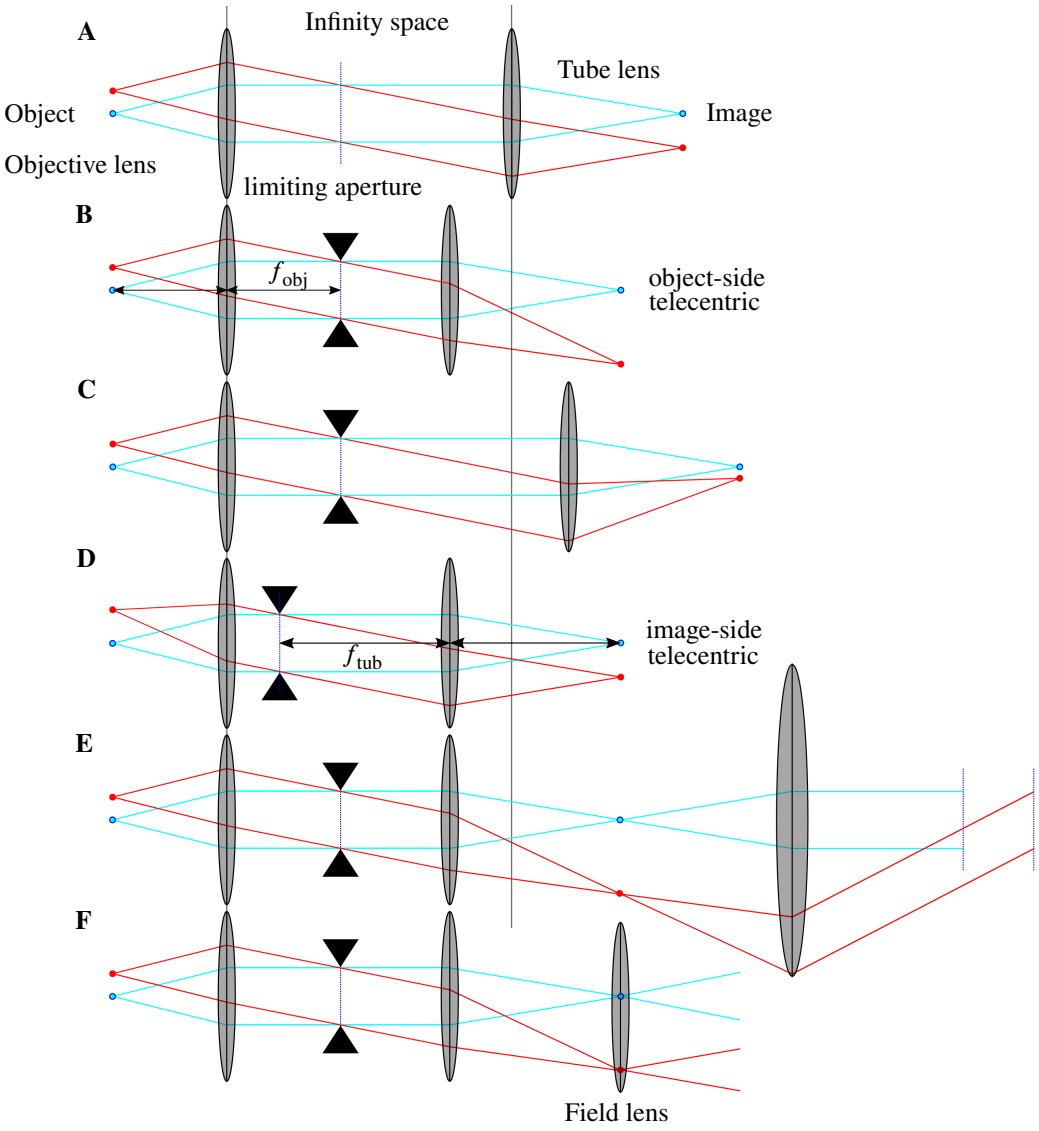

Figure 2: Telecentricity of different lens arrangements and stop positions. A description is given in the text.

as in Figure 2B, and the stop position is changed such that it is f_{tub} away from the tube lens (Figure 2D), the magnification changes when the focus on the object side changes. This system is called image-side telecentric, and is not usable for most imaging applications.

In the Ti-E, as in most commercial microscopes, the distance between the objective lens and the tube lens is about 5 cm shorter than the sum of the respective focal lengths (here: $f_{obj} = 2\,mm$, $f_{tube} = 200\,mm$). [13] As defined by the stop position at the back focal plane of the objective lens in the objective barrel, the Ti-E is only object-side telecentric. Reasons for omitting the full telecentricity in commercial microscopes are basically three-fold: (1) The image side telecentricity is not needed, as long as you keep the camera sensor at a defined position, which is standardized by the microscopes camera mount (usually an ISO C-mount [14]). (2) Nikon uses 200 mm tube lenses by default [15]. For a double-telecentric configuration, one would need over 400 mm of space between the objective and the image plane at the camera port, which would make the microscope substantially larger, increasing cost and reducing portability. (3) The objective lens collects light from each point that lies inside the opening angle of the objective lens, which is defined by its NA. Each image point creates its own specific ray bundle, which leaves the objective lens at different angles. Therefore, after the objective lens, the diameter of the collection of light beams (overall beam diameter) increases until the tube lens. By decreasing the tube length, a tube lens of smaller diameter can be used, again reducing cost.

However, the lack of image-sided telecentricity introduces two main challenges: (1) The beam diameter diverges over the whole imaging light path, creating the need to use larger aperture lenses (Figure 2E). Because lens diameters are limited, this limits the maximum length of the relay systems. However, the fixed tube lens puts lower constraints on the size of the relay systems. (2) While the Fourier plane of a central image point lies at the focal point of the Fourier transforming lens, as one would expect, the Fourier planes of image points more remote from the center are formed further back due to the diverging light cones (Figure 2E). This way the Fourier plane of the whole image is not defined any more.

Two solutions are possible: (1) The obvious one would be to place the tube lens further apart from the objective lens to restore the full telecentricity. However, the tube lens is custom fitted inside the Nikon Ti-E body and glued in place. Rising the objective lens instead would interfere with the perfect focus system and the xy-stage. (2) The only viable solution when working with a pre-assembled microscope body is to use an additional lens to correct for the diverging rays. Two positions for the field lens are possible: (1) Positioning the field lens between the tube lens and the image plane is possible, but changes the magnification of the system. (2) When the field lens is positioned directly in the image plane, no changes are made to the magnification. Therefore, the latter configuration was used. One should note that by placing a lens in the image plane, every impureness, scratch or dirt on the lens surface is imaged directly to the camera, therefore the lens should be handled with extra care and kept covered until use. Alternatively, the lens can be moved slightly off the image plane, to reduce projections of the lens body to the camera without considerably changing the magnification of the setup.

Optical aberration correction using a deformable mirror Deformable mirrors (DM) actively shape the wavefront of an incident beam. This can be used to induce a desired shape or to flatten out aberrations in the wavefront, which were induced by the sample or optical components.

Each light ray emitted in different directions by each fluorophore in the focal plane of the objective travels a unique path, first through the specimen and then trough the optics to the camera. Therefore, all these different light rays experience an individual aberration, and to perfectly correct the whole image, an individual correction for every light ray from each fluorophore would be needed. As this is impossible to realize, one makes use of the back focal plane. In principle, it does not matter whether wavefront sensing and correction are done in image or in Fourier space. The advantage of the Fourier space of a lens is, that the light coming from each fluorophore is distributed over the whole beam diameter. Wavefront sensing and correction in the Fourier plane therefore treats the global or mean aberration, which usually results in a good overall correction. [16, 17]

The piezoelectric deformable mirror uses a mirror coated glass substrate glued to a continuous piezoelectric backing plate, which is electrically divided into 40 individually addressable segments. The mirrors technical drawing is shown in Figure 12. By applying voltage to an individual segment, it changes its shape locally between convex and a concave, allowing for complex shapes of the whole mirror surface. This locally changes the optical path length and therefore the wavefront of an incident beam.

Spectral separation of the wavefront detection and sample fluorescence The samples reported here used two different fluorescent beads, a 100 nm Tetraspeck bead (TS01) for point spread function (PSF) visualization, emitting in blue, green, orange and dark red, and a much brighter 4 µm green FluoSphere bead (FS4) as a guide star for the wavefront sensor. The specimen is stained with Alexa 647. After the DM, the light path is chromatically split by a dichroic filter at 647 nm. The red part of the spectrum, including most of the specimen fluorescence as well as the red emission from the TS01 is then focused onto the camera by the lens L_{img}. The blue part, containing most of the fluorescence from FS4, is relayed again by the lenses L_{S1} and L_{S2} to form a second Fourier plane at the position of the SH.

Wavefront measurement using a Shack-Hartmann wavefront sensor The Shack-Hartman wavefront sensor (SH) was originally designed by R. Shack and J. F. Hartmann [18], and uses small lenses (lenslets) arranged in a grid array to focus collimated light onto an image sensor. [18, 19, 20] Thereby, the parallel beam is split into a number equal to the number of lenslets in the lens grit array (LGA), and each lenslet creates a small focus point on the sensor. As shown in Figure 3, the sensor area is divided into masterpixels, one for each lenslet, whereby each masterpixel consists of many subpixels. Whereas a perfect plane wave would get focused onto the subpixel in the middle of each masterpixel (Figure 3A), a distorted wavefront would get either defocused or focused onto off-center subpixels (Figure 3B). The local deviation of a beam spot δ_i from the center of the corresponding masterpixel i is directly proportional to the local slope of the WF, expressed as the derivative $\partial_{xyz}(\mathrm{WF})$. [21]

$$\delta_i \sim \partial_{xyz}(\mathrm{WF})$$

Three considerations are important for the positioning of the SH. (1) The SH should be positioned in the same plane as the DM. As placement in the Fourier plane is chosen, the creation of an additional Fourier plane is necessary. In general, two positions are possible to deflect the excitation beam out of the beam path: (1) before and (2) after the imaging lens L_{img}. Converging light reflected by a dichroic filter (DF) induces aberrations, due to the incident angle-dependent shift relative to the optical axis.[22, 23] Therefore, the dichroic filter should be placed before the imaging lens L_{img} in a parallel beam section. [24] Because the overall beam diameter is small (10 mm) at the DM and widens until it reaches L_{img}, the dichroic filter and the containing cube can be chosen to have apertures of 25 mm only, matching the commercially available standard size, when placed close to the DM. Even though this approach implicates the use of 2 additional lenses (L_{S1} and L_{S2}) and does not include L_{img} in the correction, the error is small compared to the induced aberrations when the DF is placed in the converging beam directly in front of the camera. [22]

As described, the SH uses microlenses to focus small portions of the beam from the Fourier plane to the underlying image sensor. Every point source in the image plane thereby generates a set of points on the sensor, one behind each microlens, which is called spotfield image. The location and size of a spot on its associated

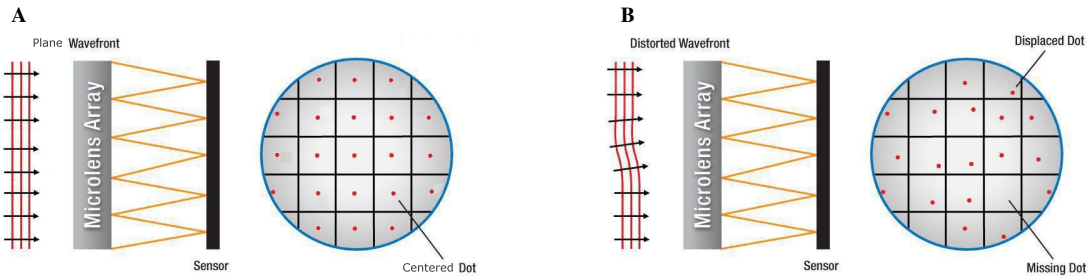

Figure 3: Working principle of a Shack-Hartmann wavefront sensor. **A** Incoming plane wave creates centered spots on each masterpixel. **B** Displaced spots resulting from an wavefront aberration. Adapted from Matitial et al. [20].

masterpixel is then used to calculate the wavefront slope at the area of the microlens. [17] Having two or more spatially separated emitters in the image plane results in two or more spots on each masterpixel. If the emitters are close and their light undergoes comparable aberration, the spots overlap and therefore still allow for a correct wavefront calculation - however, as the resulting points on the masterpixels are larger, the uncertainty in the calculation of the location may get larger. In biological samples which are labeled over a large area, every emitter generates a different spot on each masterpixel. [25] As a result, every masterpixel receives a full image of the sample, rendering a correct localization impossible. [7] To circumvent this, the wavefront measurement was restricted to a small area of the sample by inserting an aperture in the image plane in front of the SH. This cuts off all non-paraxial rays, but also reduces the number of photons reaching the sensor. As the sensitivity of the sensor is finite, a compromise was necessary and found at an opening diameter of around 0.9 mm. [16] It is also possible to use focal illumination specifically for the wavefront correction, reaching higher laser intensities in the correction area. However, the widefield illumination was found to be enough in the applications reported here.

Correction procedure As the automated closed loop control was not functional at this point, the reasons and the routine of using the AO system is described. To correct the image, first a FS4 bead was focused using the 488 nm laser only and moved to a predefined location remote the center to pass the iris in the image plane in front of the SH. Usually, the beads are bright enough to see the image of the bead on the iris. To find the optimal focal point, the wavefront of the FS4 beads was measured and the focus was moved until the defocus shown by the SH was minimized.
The Thorlabs software package for the DM and the SH features an auto-calibration to determine the relation between the measured wavefront and the voltage applied to the DM segments to correct them. [26] Unfortunately, this auto-calibration did not work before the internship. Therefore, an alternative correction procedure was used: First, the wavefront of the FS4 bead was measured and the Zernike coefficient were extracted. Next, the Zernike coefficients measured by the SH were translated to the arbitrary scale of the Zernike coefficients on the DM to initiate the correction.
The translation of the Zernike coefficients from the DM (Z_i^{DM}) to the Zernike coefficients of the SH (Z_i^{SH}) was made using the following equation:

$$Z_i^{\mathrm{DM}} = \gamma_i Z_i^{\mathrm{SH}} \,,$$

where i stands for the Zernike number.
The individual translation parameters γ_i were derived empirically by measuring the wavefront of a TS01 bead and extracting the Zernike coefficients Z_i^{SH}. Then, the PSF was manually corrected by eye using the DM until the Zernike coefficients at the SH were minimized, and the applied Zernike coefficients at the DM Z_i^{DM} were saved. To start the manual correction, Z8 and Z9 (coma) as well as Z7 and Z10 (trefoil) were used to make the PSF symmetrical in the xy-plane, while Z5 (defocus) and Z13 (spherical aberration) as well as Z6 (astigmatism) improved the symmetry in the z-direction. The Zernike numbers follow `ANSI_Z80.28-2017`. [27] After the PSF was found to be compact and symmetrical, the coefficients of the higher Zernike numbers were changed at the DM until the Zernike numbers reported by the SH were minimized.
The procedure was repeated for ten individual beads and the resulting γ_i were averaged. In general, the γ_i depend on the geometry of the excitation beam path in the system and the position of all the optical components as well as the DM and the SH and should therefore be fixed. However, the procedure was redone for every experiment session.

Limitations of the setup at the beginning of the internship As mentioned above, the main limitation of the setup was the lack of an automated closed loop control of the DM by the wavefront sensor. Instead, the correction pattern of the DM had to be manually derived before every measurement session. To locate possible reasons for the dysfunction of the closed loop control, formulation of approaches and the description of solutions are the main aims of the internship and the focus of this report.

Methods

This section is divided into two parts: (1) The rebuild setup including the modifications is described. Figure

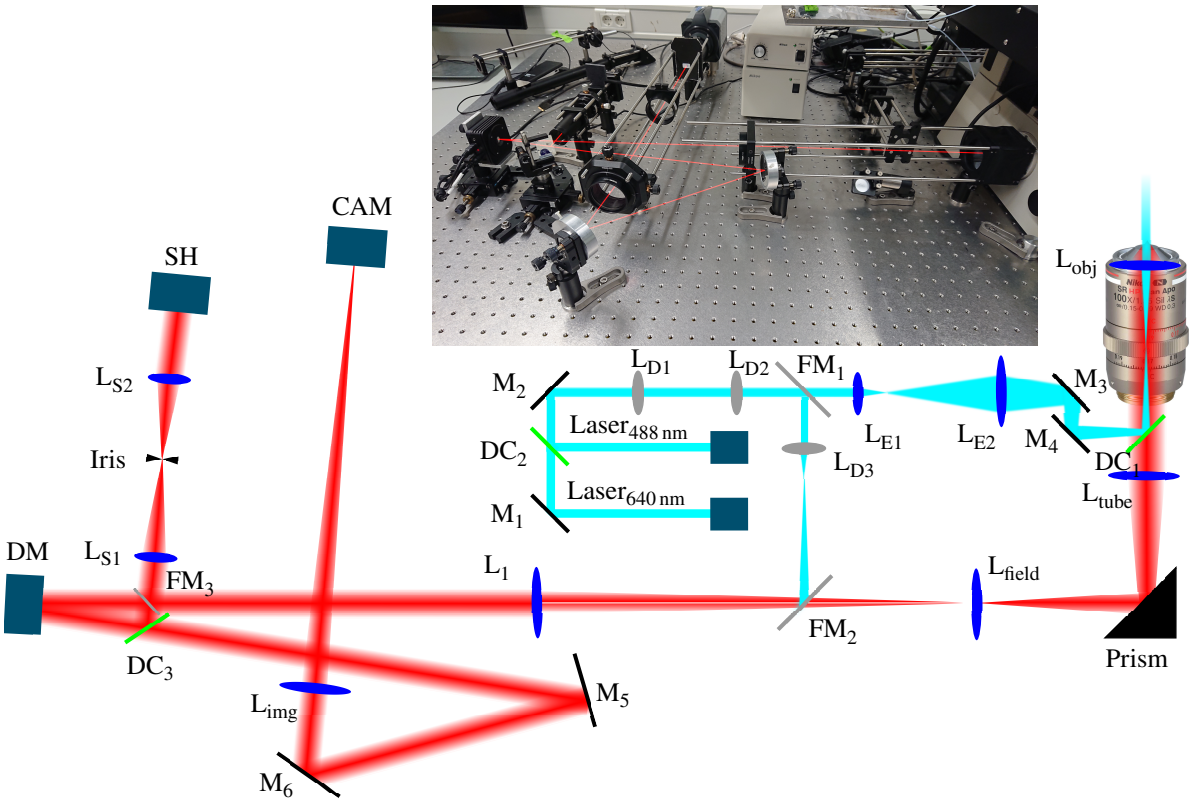

Figure 4: Simplified schematic of the light paths of the adaptive optics microscope setup with DM and SH in its final form. The excitation lasers are shown in light green and orange, and the combined beam up to the specimen is shown in light blue. The emission path from the specimen to the camera (CAM) and to the SH is shown in red. Lenses are marked in dark blue, mirrors and reflective prisms are shown in black, flip mirrors and flip lenses are drawn in grey. Dichroic filters are marked in green. The components and beam sizes are not to scale. Description of the light path in the text. Specifications of the components is in the supplementary material.
Insert: Photograph of the emission light path. Partially visible on the right is the body of the Nikon Ti-E. The leftmost component is the DM, SH and camera are in the back. All excitation light paths were fully covered in black foam board before operation to block stray light from entering the system.

4 provides an overview of the optical layout. Although the system shares details with the system presented in Figure 1, a full description is given. (2) The methods and materials are listed in detail.

Main path Lasers 1 and 2 are combined at the dichroic filter DC_2 and aligned to the TIRF/HILO rail. Lenses L_{E1} and L_{E2} on the TIRF/HILO rail focus the excitation laser onto the back focal plane of the objective. Two additional mirrors are located between L_{E2} and DC_2 on the HILO/TIRF rail to ensure enough degrees of freedom for alignment to the objective lens.
The lenses L_{E1} and L_{E2} were specified with the following considerations: (1) The sample plane should be illuminated as evenly as possible. As the beam has a Gaussian shape, a slight overfill of the FOV is considered optimal. The width of the beam in the sample plane is dependent on the collimation angle of the beam between L_{E2} and the objective back focal plane. (2) The distance between L_{E2} and the objective back focal plane should be enough to place two alignment mirrors. To get a large collimation angle over a long distance, L_{E2} is chosen to have an aperture of 50.8 mm. As L_{E1} focusses the laser beam only, a diameter of 5 mm was sufficient. The lens pair together with the objective was modeled in `Zemax` to gain the exact positions and focal lengths of 7.5 mm and 150 mm.
The objective lens picks up the specimen fluorescence and collimates the light. The width of the objective exit pupil can be calculated as: [28]

$$\varnothing_{\text{obj exit pupil}} = 2 \cdot \text{NA} \cdot f_{\text{obj}} \cdot$$

To derive the objectives focal length, one uses:

$$M_{\text{obj}} = \frac{f_{\text{tube}}}{f_{\text{obj}}} \cdot$$

With $M_{\text{obj}} = 100$, $f_{\text{tube}} = 200\,\text{mm}$ and $\text{NA} = 1.35$, the objectives exit pupil is $\varnothing_{\text{obj exit pupil}} = 5.4\,\text{mm}$.
The collimated excitation beam coming from the objective lens L_{obj} passes the infinity space in the microscope body, gets focused by the tube lens L_{tube} and reflected out of the housing of the Nikon Ti-E by the internal prism. At the first image plane, a field lens L_{field} is placed to correct for the non-telecentric placement of the tube lens and to provide a defined Fourier plane for the DM. Lens L_1 is used to collimate the light and to create the Fourier plane for the DM. L_1 was chosen to meet the following criteria: The width of the collimated beam must be

equal to the aperture size of the DM $\varnothing_{\mathrm{DM}} = 10\,\mathrm{mm}$. [42] Therefore, f_1 can be calculated by:

$$\frac{\varnothing_{\text{obj exit pupil}}}{f_{\text{tube}}} = \frac{\varnothing_{\mathrm{DM}}}{f_1} ,$$

yielding $f_1 \approx 370\,\mathrm{mm}$. As this focal length is not readily available, the lens had to be fabricated to specification. The light from the DM is split by the dichroic filter DC_3 at 647 nm. The red side of the spectrum is focused onto the camera, while the blue part is directed towards the wavefront sensor. The cutoff wavelength was chosen to leave no residue of the bright fluorescent beads in the red channel. Towards the wavefront sensor, the light is focused by L_{S1} to an iris, which is mounted in an XY-translation stage, to make the Fourier plane correspond to a single, selectable image point. After the iris, the light is collimated again by the lens L_{S2} to create the Fourier plane for the SH. Lenses

Detour path Using the flip mirrors FM_1 in front of the HILO/TIRF rail and FM_2 between $\mathrm{L}_{\mathrm{field}}$ and L_1, the laser is routed directly into the emission path for better alignment of the emission path components. In addition, lens L_{D} can be flipped into position to produce a laser beam shaped similar to the fluorescence emission, but without noticeable aberrations. This beam can be used to measure and correct the DM flatness. For alignment purposes during building of the system, an additional removable beam expander between M_2 and FM_1 was used to couple a collimated beam into L_1.

Sample Artificial samples were created with the following goals: (1) Repeatable and fast recreation of the sample. (2) A target structure which is well documented in literature for comparison. (3) A highly diffusive layer between the objective lens and the target structure as a proxy for deep tissue imaging. (4) Variable thickness of the diffusive layer to find the limits of the setup.
Two different samples were created, which are shown in Figure 5. Both samples share the general structure: (1) The bottom is sealed by a high-precision 170 µm cover glass. (2) On top of the cover glass, the diffusive layer is placed, a brain slice from male C57BL/6 mice. The hippocampal region is located over the field of view (FoV). Different slices were used, ranging in thickness from 20 to 180 µm. This induces optical aberrations of different magnitude. (3) On top of the brain slice, 100 nm TS01 and 4 µm FS4 beads are placed, submerged in the switching buffer. The switching buffer consists of 100 mmol β-mercaptoethylamine (MEA) in PBS, adjusted to PH 7.5 using potassium hydroxide (KOH). (4) Only in Sample 2, a monolayer of primary murine hippocampal neurons is laid on top of the beads. The cells are stained with Alexa Fluor 647 for α-Tubulin and come from C57BL/6 E18 mouse embryos. (5) The stack is held together with a second cover glass on the top.

Imaging modes Three different imaging modes were used to obtain the images shown in the results section of this report. (1) After the sample was mounted, the detour path was used to shape the mirror until a flat wavefront was reported on the SH. Then, the excitation light was routed back to the sample and the images were captured. In regular intervals, the mirror was checked for flatness. If significant corrections were needed, the previously captured images were dropped and captured again. Images captured in this mode are denoted "uncorrected". (2) In the second mode, the wavefront sensor and the deformable mirror working in closed loop control were used while images were captured. This mode was used for orientation on the sample to find a preferred FoV and for short acquisitions. (3) For long acquisition times above approximately 30 s, the third mode was used. After the sample was mounted and the FoV was fixed, the closed loop was turned off as soon as the mirror reached a steady state. Then, the acquisition was started and the mirror was kept steady until the acquisition finished. Then, the closed loop was reengaged. When the mirror shape initially changed significantly, the acquisition was re-done. Images acquired in mode (2) and (3) are called "corrected".

Results

The following results are presented: Figure 6, 7: PSF and wavefront images from Sample 1 are captured and the aberrations are quantified in two ways: (1) overall using the the root mean square (rms) of the wavefront (wavefront error), and (2) assigned to the aberrations using the Zernike coefficients. The system with working AO is compared against itself with a flat DM to show the improvements from the adaptive optics over a non-AO setup. Figures 8, 9: To give an approximate reference point for the abilities of the system in a scientific use-case, epifluorescence and *d*STORM images from sample 2 are presented, and the FWHM of line profiles from each image is shown. Figures 10, 11: Localization count and FWHM of line profiles is presented as a function of the thickness of the diffusion layer.

To Figure 6 Sample 1 is used with a 180 µm diffusive layer. The TS01 beads are imaged on the camera to show the PSF, while the FS4 beads are used for the wavefront measurement. The images annotated "corrected" are imaged in imaging mode 2, with the adaptive optics system in closed loop control. The images depicted "uncorrected" were obtained by switching the adaptive optics system off and returning the mirror to a flat surface, which was regularly checked using imaging mode 1.
Figure 6A shows the uncorrected PSF of the system. The projections are constructed from a 3D-stack of 90 slices. Strong manifestation of side lobes is visible, and the PSF is not symmetrical in either projection. Figure 6B shows the corrected PSF of the same bead. The shape is overall symmetric and the intensity is more centralized. Figure 6E show the uncorrected wavefront as a 2D-projection and as a 3D-render for better visualization. The uncorrected wavefront has a saddle shape, indicating high amounts of astigmatism. The wavefront rises steep at the edges, proposing spherical aberration. The asymmetry

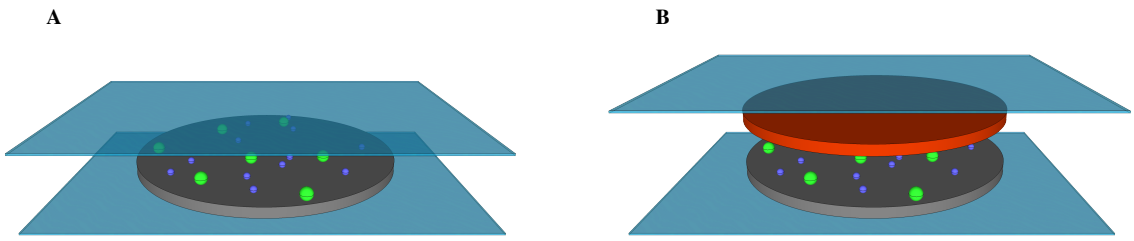

Figure 5: Structural schematic of Sample 1 (**A**) and Sample 2 (**B**). **A** and **B**: The top and bottom layers shown in transparent blue are high-precision 170 µm coverglass. The dark grey layer is a brain slice from the hippocampal region of mouse embryo. Large FS4 beads (green) and smaller TS01 beads (dark blue) sit on top of the brain slice. **B**: A primary murine neuron cell culture is shown in red. The culture is grown as a monolayer and α-Tubulin is stained with Alexa 647. Both samples are held together by water adhesion. Layers and beads are not to scale.

observed in the PSF is visible again. The wavefront error is 491 nm. In comparison, the corrected wavefront in Figure 6F only shows very small deviation from a flat plane with a wavefront error of 65 nm. The AO system reduces the wavefront error by 87 %.

To Figure 7 The Zernike coefficients were extracted from the uncorrected (red) and the corrected wavefront (grey). The uncorrected wavefront is dominated by Astigmatism, Spherical aberration, Coma and Tetrafoil, which account for over 54 % of the overall aberration. In the corrected wavefront, especially the lower Zernike numbers up to 15 experienced a strong reduction of 94 %. Over the Zernike numbers 4-66, the mean coefficients were decreased by 60 %.

To Figure 8 Sample 2 is used with a 180 µm diffusive layer. Figure 8A was recorded as a single exposure in imaging mode 2. Figure 8C was recorded as a timelapse in imaging mode 3. 8B was constructed from Figure 8C by averaging the intensity over all frames to simulate a single exposure.
Comparing the uncorrected epifluorescence image (Figure 8A) to the corrected epifluorescence image (Figure 8B), a strong improvement in contrast can be observed. Also, a projection prominent in the uncorrected epifluorescence image (Figure 8A) is moved out of focus in the corrected epifluorescence image (Figure 8B), indicating a thinner focus plane when deploying AO. Comparing the corrected epifluorescence image (Figure 8B) to the corrected *d*STORM reconstruction (Figure 8C), the typical improvements of *d*STORM are observed. *d*STORM reconstruction of the uncorrected epifluorescence image in Figure 8A was attempted, but the reconstruction algorithm failed.
The wavefront error decreases from 526 nm in Figure 8A to 49 nm in Figure 8C, marking a reduction of 91 % (wavefront not shown).

To Figure 9 20 line profiles were drawn at the same locations of Figures 8A – 8C. The lines were drawn over different projections and features of the cytoskeleton of the cells, mostly dendrites. The locations are shown in Figure 9A. Each profile was fitted with a Gaussian (Figure 9B) and the FWHM are plotted in Figure 9. The mean FWHM of the corrected *d*STORM image decreases nearly a magnitude compared to the uncorrected epifluorescence image, from (5.6 ± 0.6) µm to (0.68 ± 0.06) µm.

To Figure 10 The thickness of the diffusive medium is altered and the change in localization count for the *d*STORM reconstruction from Sample 2 is shown. `rapidSTORM` was used for the localization processing, which internally uses Poissonian maximum-likelihood estimation to fit a Gaussian model to the PSF. [29] Each timelapse was recorded with 5000 frames using 128×128 px of the camera. 5 timelapses were recorded at each slice thickness. Imaging mode 2 was used and the laser power was kept constant throughout the experiment.
The localization count appears steady up to a depth of 50 µm and then tapers off. However, the localization count of $(0.48 \pm 0.08) \times 10^6$ at 180 µm was appropriate to identify Tubulin strands and could be improved by increasing the laser power, which was intentionally kept at 100 mW to allow for the continuous experiment session.

To Figure 11 25 line profiles were drawn in *d*STORM images of Sample 2 ranging in depth from 0 to 180 µm. For each depth, a different FoV was captured and the lines were drawn over different features, mostly dendrites. The profiles were fitted with a Gaussian and the FWHM of the fits are presented in Figure 11. The FWHM increases steadily from (0.6 ± 0.3) µm without a brain slice up to (1.4 ± 0.3) µm with the 180 µm slice.

Discussion

In summary, a more straightforward quantification of wavefront data was possible with Sample 1. A reduction in wavefront error of up to 90 % can be reported when imaging 4 µm green beads through 180 µm unstained murine hippocampal tissue. Effective reduction of the leading aberrations like astigmatism and spherical aberration could be shown in these samples, also counting a reduction of over 90 % of the first 11 Zernike coefficients (ignoring piston, tip and tilt). In contrast, the tubulin images from Sample 2 were only quantified using line pro-

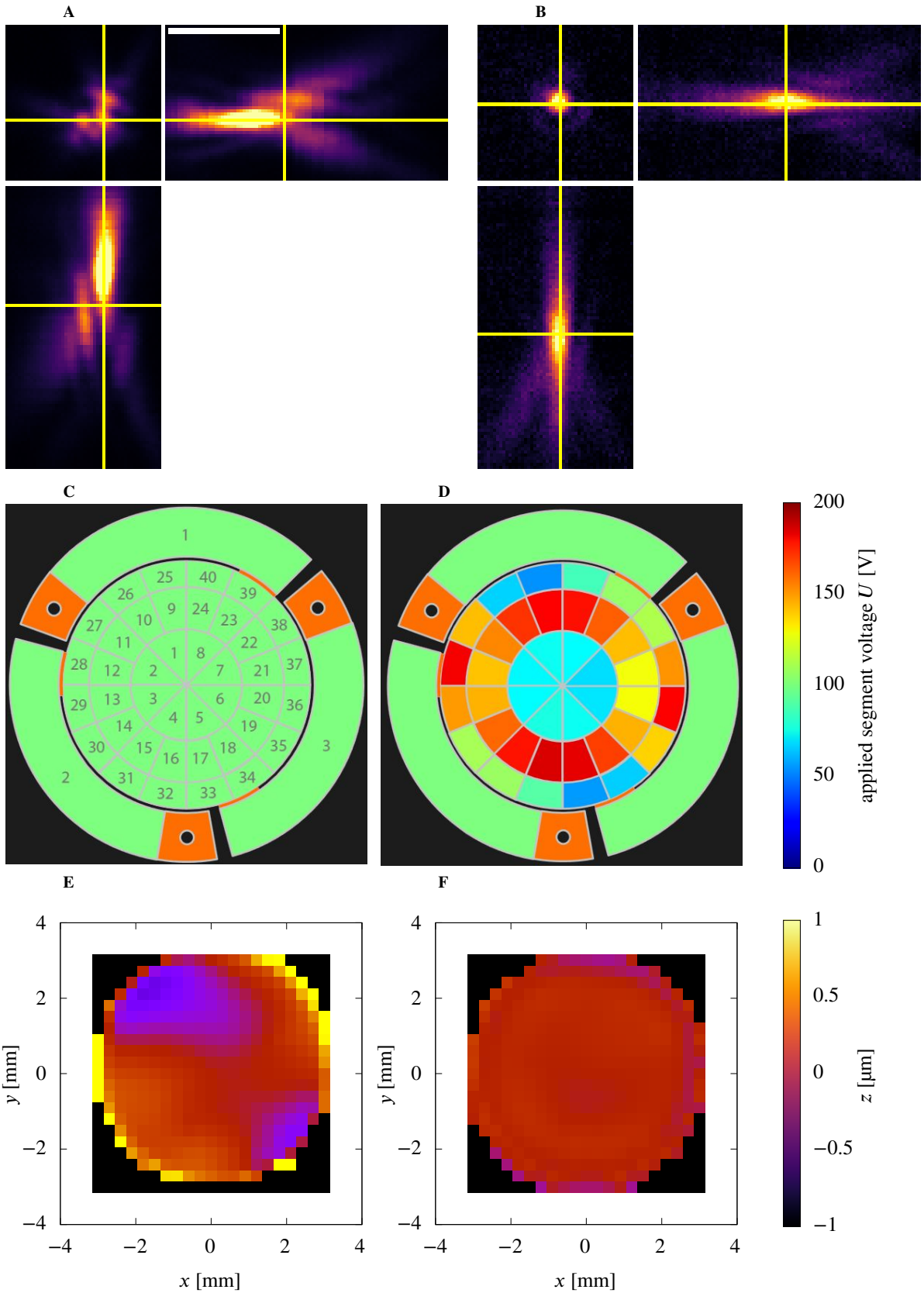

Figure 6: PSF, DM pattern and wavefront of Sample 1, imaged through a 180 µm brain slice with and without AO. **A**, **B** PSF of a single TS01 bead uncorrected (**A**) and corrected (**B**). *xy*-, *xz*- and *yz*-projections are shown. Scale bar is 2 µm for all projections of the PSF. **C** DM in resting position with 100 V applied to each segment. Actual flatness of the mirror surface was checked as described in the detour path paragraph. **D** Voltage applied to the DM segments during the correction. **E**, **F** Wavefront of the same TS01 bead as shown in **A** and **B** uncorrected (**E**) and corrected (**F**).

files over arbitrary features of the cytoskeleton. As these images are not 3D images, large ambiguity about true di-

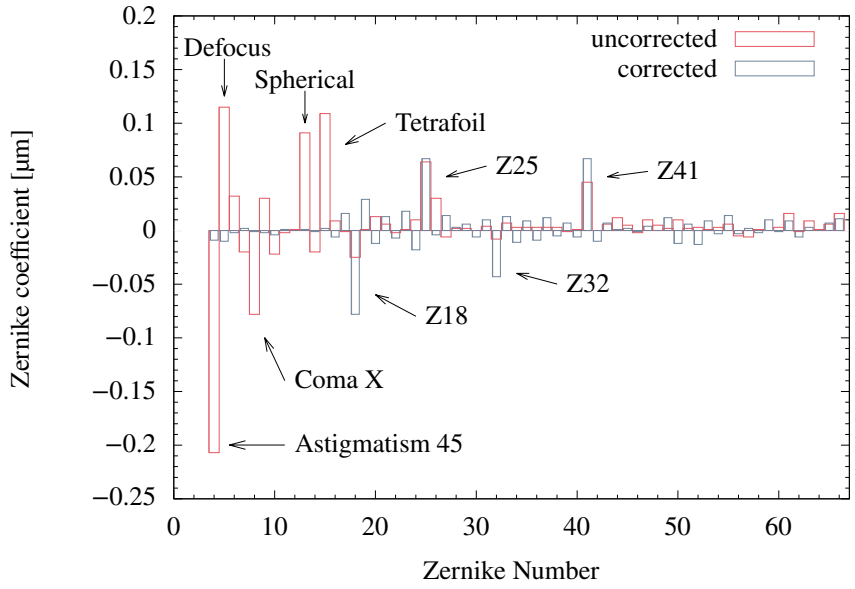

Figure 7: Coefficients for the Zernike numbers 4 – 66, compared between uncorrected and corrected epifluorescence images of a single TS01 bead. The graph shows a single, exemplary measurement, but is considered representative here. The allocation of the Zernike numbers follows `ANSI_Z80.28-2017`. [27].

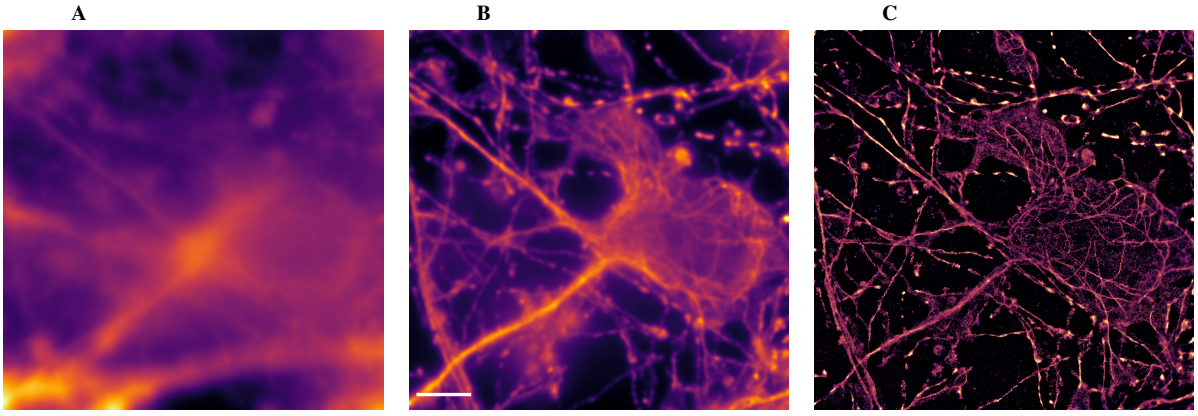

Figure 8: Comparison of a an uncorrected epifluorescence image (**A**), a corrected epifluorescence image (**B**) and a *d*STORM image (**C**) of the same field of view of Sample 2, using 180 µm brain slice thickness. The *d*STORM reconstruction was executed by `rapidSTORM`. [29] Epifluorescent images were recreated from the timelapse by averaging the intensity over all frames of the time-lapse. For the images shown in Figure 8, a 256×256 px, 15×10^3 frames fast timelapse was captured. The 640 nm laser was used in a HILO illumination at $\approx 50\,\mathrm{kW\,cm^{-2}}$. Scale bar is 2 µm and valid for all three images.

sample	emitter	imaging depth [µm]	uncorrected [nm]	corrected [nm]	author
drosophila embryo	647 nm bead	20	104	-	Azucena et al.
drosophila embryo	red bead	-	151	-	Tao et al.
drosophila larvae	yolk autofluorescence	-	387	-	Tao et al.
	backscattered laser	-	190	10	Bourgenot et al.
amyloid plaques	-	170	-	-	Mlodzianoski et al.
endothelial cells	-	100	52	-	Zheng et al.
murine hippocampus	515 nm bead	180	491	65	reported here
murine hippocampus	515 nm bead	180	526	49	reported here

Table 1: Collection of literature reported data of uncorrected and corrected wavefront error. [25, 30, 31, 32, 33, 34, 35]

mensions of these features remains. A non-linear decay of the image quality with rising imaging depth is presented for *d*STORM images images through 180 µm of unstained murine hippocampal tissue. The image quality is quantified by localization count of the *d*STORM algorithm and FWHM of projections in the *d*STORM

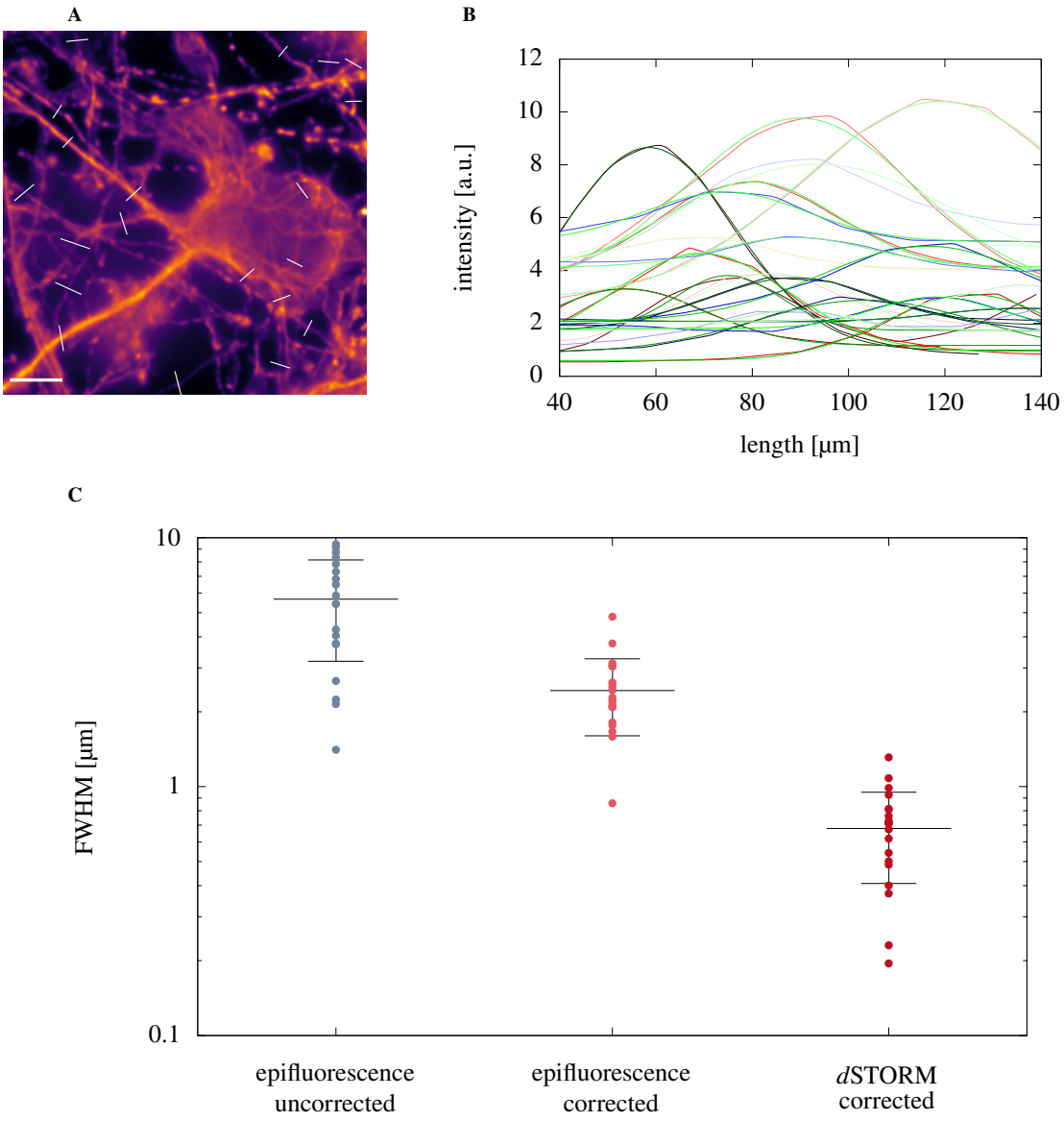

Figure 9: Line profiles were obtained from the three images shown in 8 to compare the FWHM of their fits. **A** 20 line profile locations, exemplary drawn over the epifluorescent AO image. **B** The line profiles from Figure 9A are shown exemplary with their corresponding fits. **C** The FWHM of the fits obtained in 9B for the three images shown in Figure 8. Lines represent mean value and standard deviation.

image.

Setup modifications In summary, the initial setup lacked functioning closed loop control, and wavefront corrections could only be made by hand. The main reasons are the following: (1) The pupils at the DM and the SH were not correctly sizes according to the apertures of the instruments. Thorlabs, the vendor for both instruments do not report the maximum accepted deviation of the beam width at the DM and WFS. For the setup presented here, deviation of more than $\approx 10\,\%$ render the system non-functional. Recalculation of the relay systems and a custom made lens solved this problem. (2) Especially when using non-telecentric optics like a commercial microscope body, caution must be taken when installing optical components with a restricted clear aperture. For the system reported here, the relay between the SH and the DM was using 25.4 mm diameter lenses, which were clipping the beam. The issue was found by placing a bright fluorescent slide on the objective lens, which made reflections from the beam visible to the bare eye. Routing a laser into the excitation path is not sufficient in this case, as the beam will only emulate a single fluorescent emitter in the center of the sample plane and not account for off-axis emitters. The off-axis emitters (shown in red in Figure 2) contribute substantially to the width of the beam, most notably at the location of relay lenses. When beam clipping occurs, two solutions are possible: (1) Choosing larger aperture optics, which are often more expensive, or (2) choosing shorter relays with shorter focal length lenses, which shortens the length at which the beam increases in size.

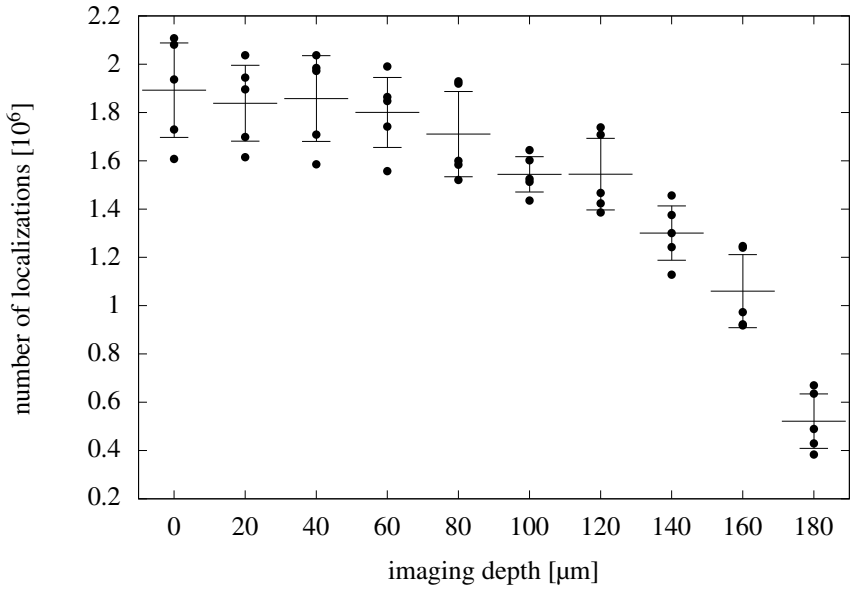

Figure 10: Number of localizations detected by the localization algorithm from *d*STORM images taken at different imaging depths. Sample 2 was used. Error bars indicate standard deviation.

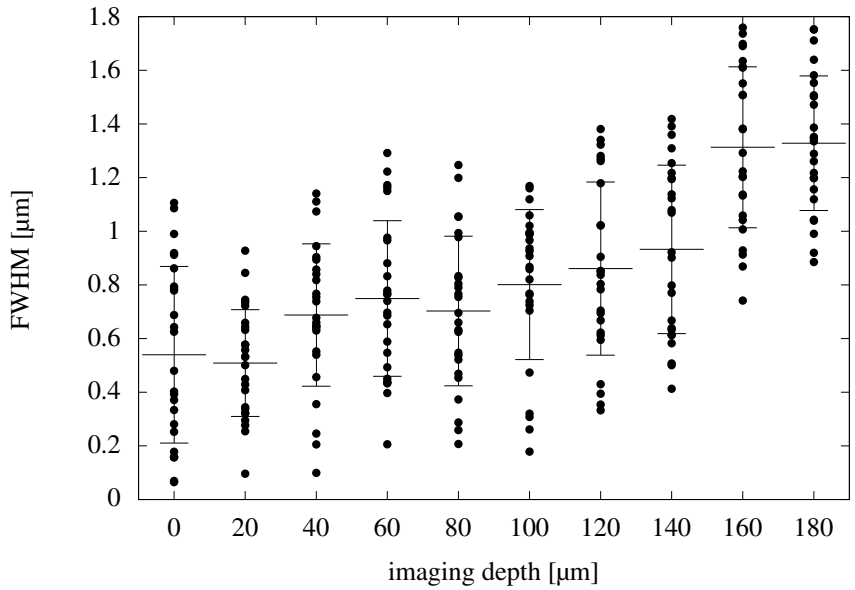

Figure 11: Full width at half maximum (FWHM) of fitted line profiles from *d*STORM images taken at different imaging depths. Sample 2 was used. Error bars indicate standard deviation.

Wavefront error To take wavefront errors into perspective, Table 1 was compiled using the data reported here as well as reports from literature. Azucena et al. [30, 31] imaged fluorescent beads embedded 20 µm deep in drosophila embryos and used active wavefront sensing. The average wavefront error of an uncorrected image was reported to be 104 nm, compared to 491 nm in Figure 6A and 526 nm in Figure 8A reported here. The residual wavefront error of the corrected images is 65 nm in Figure 6B and 49 nm in Figure 8C, demonstrating a reduction of 87 % and 91 %, respectively. The group used red fluorescent beads (peak emission at 647 nm), which undergo less optical aberrations. The leading aberrations were reported as spherical aberration, coma and astigmatism, which can be confirmed here in Figure 7. Tao et al. [32] were able to correct an wavefront error of 151 nm, also in drosophila larvae, using active wavefront sensing of red fluorescent beads. The same group also showed that autofluorescence in the drosophila yolk can be used as a guide star for the SH, where they reported correction of 387 nm wavefront error. [33] Bourgenot et al [25] used backscattered laser light as an alternative guide star to circumvent the need to inject beads. They archieved wavefront improvements from 190 µm down to 10 µm. Mlodzianoski et al [34] imaged amyloid plaques in mouse frontal cortex up to a depth of 170 µm using sensorless AO. Unfortunately, no wavefront error is reported. As the tissue sample is comparable in optical properties, a high wavefront error could be possible. Zheng et al. [35] corrected a wavefront error of 52 nm

at a depth of 100 µm for Rhodamine–phalloidin-stained actin filaments in primary mouse endothelial cells using active sensing of fluorescent beads.
In general, one can see that our wavefront error in the uncorrected image is large compared to the values reported in literature, indicating that the murine brain tissue reported here induces large optical aberrations. The residual wavefront error was found to be still higher than many values reported in literature, especially compared to sensorless approaches. However, authors using sensorless AO consistently used less aberrating samples and showed less wavefront error reduction compared to their wavefront error starting value.

Software In the results, no corrected 3D *d*STORM image is presented. The reason is as follows: The AO software used to control the SH and DM is not capable of applying an additional static, defined mirror pattern on top of the dynamic closed loop correction pattern. An additional pattern is useful for two reasons: (1) As a flatfield correction to accommodate static aberrations caused by optical components which are not part of the closed loop. For example, aberrations induced by L_{E1} and L_{E2} should be subtracted from the correction, and aberrations induced by L_{img} should be added to the correction pattern of the DM. (2) To induce a defined astigmatism to allow for 3D *d*STORM imaging while the control loop is closed. The addition of a cylinder lens would allow this, however, the astigmatism produced by a DM is more sophisticated and customizable and would be preferred over a cylinder lens. [36]
With broad help from members of the Dynamic Optics and Photonics group, an attempt to custom write a control software in `Python` has been made. The AO software package provided by Thorlabs includes drivers for `C` compilers, `LabVIEW`, `.Net`, and `DataSocket` support, making modifications possible. A collection of `Python` device wrappers was made available by Jacopo Antonello, involving the Thorlabs Camera used for the SH. [37] Jiahe Cui was working on `SenAOReFoc`, a `Python` AO control software. [38] Implementing support for the Thorlabs SH and DM should be possible. Also, Karen Hampson shared a `C` program for DM control. Due to limited documentation of the Thorlabs DM, low use in microscopy systems, and the time frame of this internship, the attempt to write a custom software did not succeed.

Conclusion

Documentation exists on alignment procedures and technical considerations for the implementation of AO in superresolution microscopy. [17, 39, 40] However, finding the causes of failure of a complex system involves both theoretical understanding and practical experience. Here, some information is given which potentially helps in the construction and alignment process, and the abilities of the functioning system are demonstrated. In the future, a custom software for the AO system would enable AO corrected 3D *d*STORM imaging of large biological samples for whole-cell visualization.

Acknowledgement

I want to thank Martin Booth for accepting the internship and providing generous help throughout the process of troubleshooting and rebuilding the *d*STORM setup. Thank you for the ability to connect to a lot of very skilled people from your lab. Especially, I want to thank Jingyu Wang as my supervisor, who quickly identified and solved most of the problems with the setup. You provided very useful and practical insights from AO and microscopy in general. I also want to thank Markus Sauer for uneventful providing the laboratory and funding all purchases needed for the initial setup and this rebuild. I enjoyed the community you have grown around your lab. Last, I want to thank Gerti Beliu and Andreas Kurz for supervision and support, especially in the building phase of the initial setup at the Biocenter Würzburg.

References

[1] L. Groß. “Point-spread function engineering for single-molecule localization microscopy in brain slices”. MA thesis. 2021. DOI: 10.25972/OPUS-28259.

[2] M. Heilemann et al. “Subdiffraction-Resolution Fluorescence Imaging with Conventional Fluorescent Probes”. In: *Angewandte Chemie International Edition* 47.33 (2008), pp. 6172–6176. DOI: 10.1002/anie.200802376.

[3] J. Foelling et al. “Fluorescence nanoscopy by ground-state depletion and single-molecule return”. In: *Nature Methods* 5.11 (Nov. 2008), pp. 943–945. ISSN: 1548-7105. DOI: 10.1038/nmeth.1257.

[4] S. van de Linde et al. “Direct stochastic optical reconstruction microscopy with standard fluorescent probes”. In: *Nature protocols* 6.7 (June 2011), pp. 991–1009. ISSN: 1754-2189. DOI: 10.1038/nprot.2011.336.

[5] M. J. Booth. “Adaptive optical microscopy: the ongoing quest for a perfect image”. In: *Light: Science &Amp; Applications* 3 (Apr. 2014). Review, p. 165. DOI: 10.1038/lsa.2014.46.

[6] M. Booth et al. “Aberrations and adaptive optics in super-resolution microscopy”. In: *Microscopy* 64.4 (June 2015), pp. 251–261. ISSN: 2050-5698. DOI: 10.1093/jmicro/dfv033.

[7] D. Burke et al. “Adaptive optics correction of specimen-induced aberrations in single-molecule switching microscopy”. In: *Optica* 2.2 (Feb. 2015), pp. 177–185. DOI: 10.1364/OPTICA.2.000177.

[8] *Nikon Ti-E inverted Reseach Microscope Operation Manual*. Nikon. 2020.

[9] *NIS-Elements*. Nikon. 2020. URL: https://www.nikon.com/products/microscope-solutions/lineup/img_soft/nis-elements/ (visited on 01/01/2021).

[10] *Nikon Objectives*. Nikon Corporation. 2020. URL: https://www.microscope.healthcare.nikon.com/de_EU/selectors/objectives (visited on 10/06/2020).

[11] M. Tokunaga, N. Imamoto and K. Sakata-Sogawa. "Highly inclined thin illumination enables clear single-molecule imaging in cells". In: *Nature Methods* 5.2 (Feb. 2008), pp. 159–161. ISSN: 1548-7105. DOI: 10.1038/nmeth1171.

[12] A. L. Stout and D. Axelrod. "Evanescent field excitation of fluorescence by epi-illumination microscopy". In: *Applied optics* 28.24 (1989), pp. 5237–5242. DOI: 10.1364/AO.28.005237.

[13] S. Ross. *Microscopy: Disassembling a Nikon Ti Eclipse*. Nikon. URL: https://www.youtube.com/watch?v=DAV0X1c3s-g#t=30m59s (visited on 30/12/2020).

[14] ISO/TC 172/SC 5 Microscopes and endoscopes. *Microscopes — Interfacing connection type C*. ISO 10935:2009. International Organization for Standardization, Aug. 2009.

[15] *Infinity Optical Systems*. Nikon Corporation. 2020. URL: https://www.microscopyu.com/microscopy-basics/infinity-optical-systems (visited on 04/02/2020).

[16] A. B. Vasista, D. K. Sharma and G. P. Kumar. "Fourier Plane Optical Microscopy and Spectroscopy". In: *digital Encyclopedia of Applied Physics*. American Cancer Society, 2019, pp. 1–14. ISBN: 9783527600434. DOI: 10.1002/3527600434.eap817.

[17] D. Wilding et al. "Practical guidelines for implementing adaptive optics in fluorescence microscopy". In: 10502 (2018). Ed. by T. G. Bifano, J. Kubby and S. Gigan, pp. 92–103. DOI: 10.1117/12.2287647.

[18] B. C. Platt and R. B. Shack. "History and principles of Shack-Hartmann wavefront sensing." In: *Journal of refractive surgery* 17 5 (2001), pp. 573–577.

[19] M. Downing et al. "Review of AO Wavefront Sensing Detectors". In: (Mar. 2016). URL: https://www.eso.org/sci/meetings/2009/dfa2009/Writeups/WR-Downing_AOWFS_DfA2009.pdf.

[20] R. P. Matital et al. "Review of holographic wavefront sensors". In: (Jan. 2018), pp. 535–538. DOI: 10.1109/EIConRus.2018.8317153.

[21] M. E. Khosroshahi. "Study of spatial thermal distribution of gold nanourchins in saline by combined transverse probe beam deflection and beam wavefront sensor: biomedical implications". In: *Applied Physics B* 125.12 (Nov. 2019), p. 229. ISSN: 1432-0649. DOI: 10.1007/s00340-019-7338-1.

[22] V. J. Doherty and D. Shafer. "Simple Method Of Correcting The Aberrations Of A Beamsplitter In Converging Light". In: *1980 International Lens Design Conference*. Ed. by R. E. Fischer. Vol. 0237. International Society for Optics and Photonics. SPIE, 1980, pp. 195–201. DOI: 10.1117/12.959086.

[23] J. Pawley, ed. *Handbook of Biological Confocal Microscopy*. 3rd ed. Springer US, 2006, pp. 212–213. ISBN: 978-0-387-45524-2. DOI: 10.1007/978-0-387-45524-2.

[24] B. Dong and M. J. Booth. "Wavefront control in adaptive microscopy using Shack-Hartmann sensors with arbitrarily shaped pupils". In: *Opt. Express* 26.2 (Jan. 2018), pp. 1655–1669. DOI: 10.1364/OE.26.001655.

[25] C. Bourgenot et al. "Comparison of closed loop and sensorless adaptive optics in widefield optical microscopy". In: *Journal of the European Optical Society - Rapid publications* 8.0 (2013). URL: https://www.jeos.org/index.php/jeos_rp/article/view/13027.

[26] *Deformable Mirror Software*. Thorlabs. 2020. URL: https://www.thorlabs.de/software_pages/ViewSoftwarePage.cfm?Code=DMP40 (visited on 01/01/2021).

[27] Ophthalmics. *Optical Aberrations of Eyes*. ANSI Z80.28. American National Standard Institute, 2017.

[28] *Pupil Diameter and Beam Spot Diameter of Objective Lens*. Olympus. 2020. URL: https://www.olympus-ims.com/en/microscope/terms/luminous_flux/ (visited on 04/02/2020).

[29] S. Wolter et al. "rapidSTORM: accurate, fast open-source software for localization microscopy". In: *Nature Methods* 9.11 (Nov. 2012), pp. 1040–1041. ISSN: 1548-7105. DOI: 10.1038/nmeth.2224.

[30] O. Azucena et al. "Implementation of adaptive optics in fluorescent microscopy using wavefront sensing and correction". In: *MEMS Adaptive Optics IV*. Ed. by S. S. Olivier, T. G. Bifano and J. A. Kubby. Vol. 7595. International Society for Optics and Photonics. SPIE, Feb. 2010, pp. 131–139. DOI: 10.1117/12.846380.

[31] O. Azucena et al. "Wavefront aberration measurements and corrections through thick tissue using fluorescent microsphere reference beacons". In: *Opt. Express* 18.16 (Aug. 2010), pp. 17521–17532. DOI: 10.1364/OE.18.017521.

[32] X. Tao et al. "Adaptive optics confocal microscopy using direct wavefront sensing". In: *Opt. Lett.* 36.7 (Apr. 2011), pp. 1062–1064. DOI: 10.1364/OL.36.001062.

[33] X. Tao et al. "Adaptive optical two-photon microscopy using autofluorescent guide stars". In: *Opt. Lett.* 38.23 (Dec. 2013), pp. 5075–5078. DOI: 10.1364/OL.38.005075.

[34] M. J. Mlodzianoski et al. "Active PSF shaping and adaptive optics enable volumetric localization microscopy through brain sections". In: *Nature Methods* 15.8 (2018), pp. 583–586. ISSN: 1548-7105. DOI: 10.1038/s41592-018-0053-8.

[35] W. Zheng et al. "Adaptive optics improves multiphoton super-resolution imaging". In: *Nature Methods* 14 (June 2017), p. 869. DOI: 10.1038/nmeth.4337.

[36] A. Kurz. "Correlative live and fixed cell superresolution microscopy". PhD thesis. 2020. DOI: 10.25972/OPUS-19945.

[37] J. Antonello. *Collection of Device Wrapper*. URL: https://github.com/jacopoantonello/devwraps.

[38] J. Cui et al. "SenAOReFoc: A Closed-Loop Sensorbased Adaptive Optics and Remote Focusing Control Software". 2021. DOI: 10.48550/ARXIV.2112.10576.

[39] K. M. Hampson et al. *Practical Implementation of Adaptive Optical Microscopes*. 2020. DOI: 10.5281/zenodo.4080673. URL: https://aomicroscopy.org/ (visited on 01/01/2021).

[40] N. Hall et al. "Microscope-AOtools: a generalised adaptive optics implementation". In: *Opt. Express* 28.20 (Sept. 2020), pp. 28987–29003. DOI: 10.1364/OE.401117.

[41] *Shack Hartman Wavefront Sensor Operation Manual*. Thorlabs GmbH. 2020.

[42] *Piezoelectric Deformable Mirror (DMP40) Operation Manual*. Thorlabs GmbH. 2021.

[43] *What is an Electron Multiplying CCD (EMCCD) Camera*. Oxford Instruments. 2020. URL: https://andor.oxinst.com/learning/view/article/electron-multiplying-ccd-cameras (visited on 22/05/2020).

[44] *Toptica488*. Toptica Photonics. 2020. URL: https://www.toptica.com/products/single-mode-diode-lasers/ibeam-smart (visited on 21/11/2021).

[45] *gem 640*. Laser Quantum. 2020. URL: https://www.laserquantum.com/products/detail.cfm?id=135 (visited on 09/06/2020).

[46] *quad-band dichroic filter*. Chroma Technology Corp. 2020. URL: https://www.chroma.com/products/parts/zt405-488-561-640rpc (visited on 09/06/2020).

[47] *ZT 532 rdc dichroic filter*. Chroma Technology Corp. 2020. URL: https://www.chroma.com/products/parts/zt532rdc (visited on 09/06/2020).

[48] *BLP01 647R 25 dichroic filter*. IDEX Health & Science, LLC. 2020. URL: https://www.semrock.com/filterdetails.aspx?id=blp01-647r-25 (visited on 20/01/2022).

[49] *TetraSpeck Microspheres*. ThermoFisher Scientific. 2020. URL: https://www.thermofisher.com/order/catalog/product/T7279#/T7279 (visited on 14/03/2020).

[50] *FluoSpheres Sulfate Microspheres*. ThermoFisher Scientific. 2020. URL: https://www.thermofisher.com/order/catalog/product/F8859#/F8859 (visited on 14/03/2020).

[51] *Alexa 647*. ThermoFisher Scientific. 2020. URL: https://www.thermofisher.com/de/en/home/life-science/cell-analysis/fluorophores/alexa-fluor-647.html (visited on 09/06/2020).

[52] T. Williams and C. Kelley. *Gnuplot 5.0*. 2020. URL: http://www.gnuplot.info/ (visited on 01/01/2021).

Supplementary materials

The specifications are given for the redesigned, final setup.

Wavefront sensor

name	WFS30-7AR/M
manufacturer	Thorlabs
type	Shack-Hartmann wavefront sensor
microlens array name	MLA 150-7AR
microlens aperture	11.5×7.5 mm
number of microlenses	73×45
microlens pitch	150 µm
microlens diameter	146 µm
sensor type	CMOS
resolution	1936 × 1216 px
pixel size	5.83 µm^2

Table 2: Specifications of the wavefront sensor used in the setup. [41]

Deformable mirror

name	DMP 40/M-P01
manufacturer	Thorlabs
type	piezoelectric deformable mirror
number of actuators	40
coating	protected silver
reflectance (450 – 2000 nm)	> 97.5 %
voltage range per segment	0 – 200 V

Table 3: Specifications of the deformable mirror used in the setup. [42]

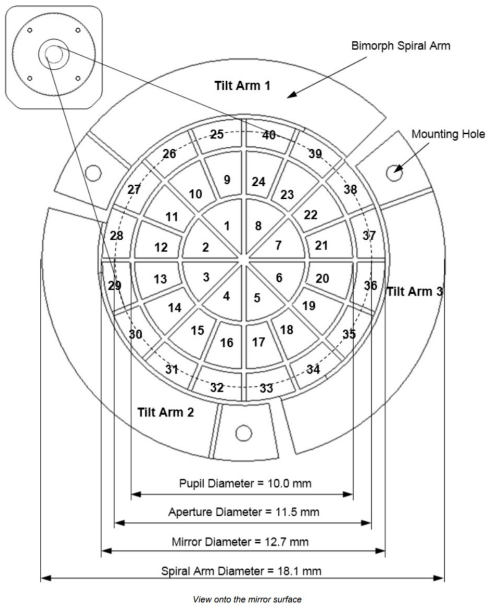

Figure 12: Technical drawing of the mirror segments. The optimal pupil is shown as a dashed line. Image source: Thorlabs `DMP40_M-P01` Manual, version 2.7. [42]

Camera

name	Andor Sona 4.2B-11
manufacturer	Oxford Instruments
sensor type	back-illuminated sCMOS
sensor size	22.5×22.5 mm
resolution	2048×2048 px
pixel size	11 µm
bit depth	16

Table 4: Specifications of the camera used in the setup. [43]

Lasers

name	wavelength	manufacturer	power [mW]
iBeamSmart 488 S HP	488	Toptica	200
gem 640	640	Laserquantum	550

Table 5: Specifications of the lasers used in the setup. [44, 45]

Filters

abbreviation	name	manufacturer	λ cut-on / cut-off [nm]
DC_1	zt405/488/561/640rpc flat	Chroma	405/488/561/640
DC_2	ZT532rdc	Chroma	532
DC_3	BLP01-647R-25	Semrock	647

Table 6: Specifications of the filters used in the setup. [46, 47, 48]

Fluorescent microspheres

abbreviation	∅ [µm]	EX [nm]	EM [nm]	manufacturer	Full name
TS01	0.1	360/505/560/660	430/515/580/680	ThermoFisher	TetraSpeck
FS4	4	505	515	ThermoFisher	FluoSpheres Sulfate

Table 7: Specifications of the fluorescent microspheres. [49, 50] EX: excitation maxima. EM: emission maxima.

Spectral overview

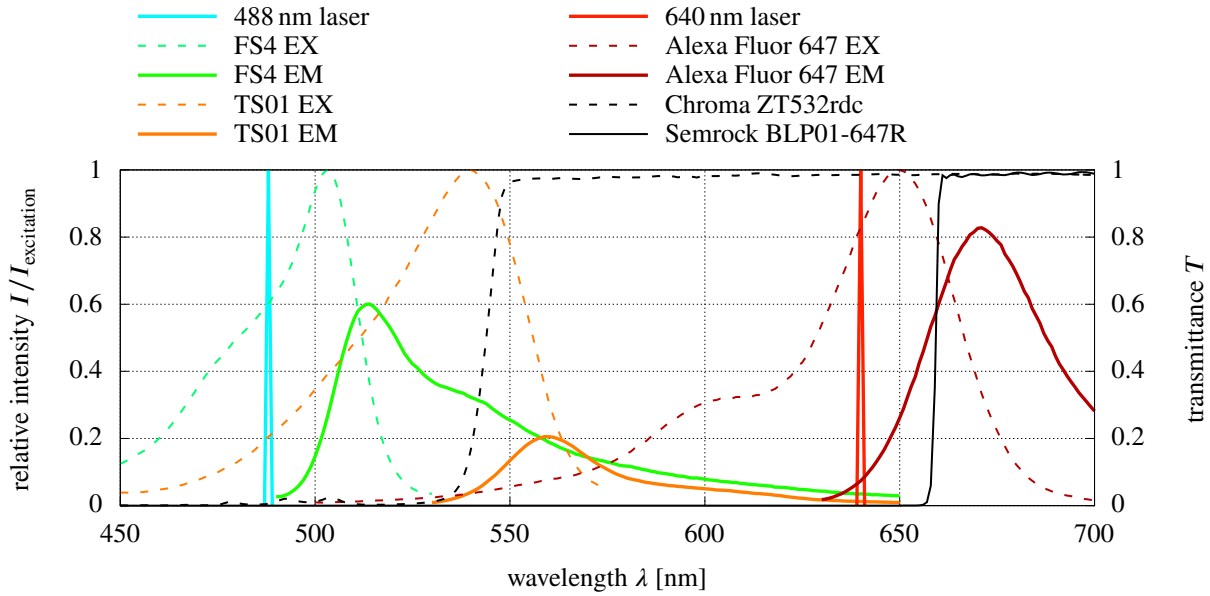

Figure 13: Spectral overview of the beads, the dye and the lasers as well as the dichroic filters used. Laser intensity as well as the excitation spectra (EX) are normalized. Emission (EM) of Alexa Fluor 647 is shown relative to the 640 nm excitation, while the emission of the FS4 and the TS01 beads is shown relative to the 488 nm excitation. For the TS01, only the orange dye is shown. Data was taken from [44, 45, 47, 48, 49, 50, 51]

.

Lenses

abbreviaton	name	manufacturer	focal length [mm]	lens type	diameter [mm]
L_{E1}	AC050-008-A-ML	Thorlabs	7.5	achromatic doublet	5
L_{E2}	AC508-150A-ML	Thorlabs	150	achromatic doublet	50.8
L_{tube}		Nikon	200	apochromatic multi-element	36
L_{obj}	SR HP Plan Apo 100X/1.35 Sil λS	Nikon	2	apochromatic multi-element	
L_{field}	AC508-750A-ML	Thorlabs	750	achromatic doublet	50.8
L_1	DLB-50-370PM-LC	OptoSigma	370	achromatic doublet	50.8
L_{S1}	AC254-100-A-ML	Thorlabs	100	achromatic doublet	25.4
L_{S2}	AC254-075-A-ML	Thorlabs	75	achromatic doublet	25.4
L_{img}	AC508-750-A-ML	Thorlabs	750	achromatic doublet	50.8

Table 8: Specifications of the lenses used in the setup

Mirrors

name	name	manufacturer	mirror type	reflective band nm	diameter [mm]
M_1 - M_4, FM_1 - FM_3	BB1-EO2	Thorlabs	dielectric	400-750	25.4
M_5, M_6	BB2-EO2	Thorlabs	dielectric	400-750	50.8

Table 9: Specifications of the mirrors used in the setup

Reagents

reagent	manufacturer	order number
α-Tubulin staining		
glutaraldehyde (GA)	Sigma-Aldrich	G5882
Triton X-100	ThermoFischer	28314
carbonate-bicarbonate-buffer (CB)		
PBS	Sigma-Aldrich	D1408
sodium borohydrate $NaBH_4$		
bovine serum albumin (BSA)	Sigma-Aldrich	A3983
rabbit anti-α-tubulin	ThermoFischer	A11126
goat anti rabbit Alexa Fluor 647	ThermoFischer	A27040
formaldehyde	Sigma-Aldrich	F8775
Poly-D-Lysine (PDL)	Sigma-Aldrich	P6407
Switching buffer		
PBS	Sigma-Aldrich	D1408
β-mercaptoethylamine (MEA)	Sigma-Aldrich	M6500
Potassium hydroxide	Sigma-Aldrich	60377
General		
coverglass	Carl Roth	LH23.1

Table 10: Specifications of reagents used in the setup

Fitting Algorithm

Fits of the line profiles were performed using `Gnuplot` [52] for the Gaussian function

$$f(x) = \frac{c}{\sigma\sqrt{2\pi}} \exp\left(\frac{-(x-\mu)^2}{2\sigma^2}\right) + b\,, \tag{1}$$

having σ, μ, b and c as free variables. Starting values for the fits were set manually for each individual fit and all fits were checked by eye to ensure proper conversion of the fitting routine. The FWHM was then calculated from σ using:

$$\mathrm{FWHM} = 2\sqrt{2\ln 2}\,\sigma\,. \tag{2}$$

The maximum intensity I was calculated by:

$$I = \frac{c}{\sigma\sqrt{2\pi}}\,. \tag{3}$$